

RIS-aided Wireless Communications: Can RIS Beat Metal Plate?

Jiangfeng Hu, Haifan Yin, Li Tan, Lin Cao, Xilong Pei

Abstract—Reconfigurable Intelligent Surface (RIS) has recently been regarded as a paradigm-shifting technology beyond 5G, for its flexibility on smartly adjusting the response to the impinging electromagnetic (EM) waves. Usually, RIS can be implemented by properly reconfiguring the adjustable parameters of each RIS unit to align the signal phase on the receiver side. And it is believed that the phase alignment can be also mechanically achieved by a metal plate with the same physical size. However, we found in the prototype experiments that, a well-rotated metal plate can only approximately perform as well as RIS under limited conditions, although its scattering efficiency is relatively higher. When it comes to the case of spherical wave impinging, RIS outperforms the metal plate even beyond the receiving near-field regions. We analyze this phenomenon with wave optics theory and propose explicit scattering models for both the metal plate and RIS in general scenarios. Finally, the models are validated by simulations and field measurements.

Index Terms—Reconfigurable intelligent surfaces, Scattering model, Wave optics theory.

I. INTRODUCTION

Reconfigurable Intelligent Surface (RIS) is widely believed to be a promising technology for its capability of smartly configure the impinging EM waves with a large number of sub-wavelength-sized passive scattering units [1]. A series of application scenarios have been investigated under different assumptions [2]. However, the RIS technology is still in its infancy, since the actual physical characteristics, the efficient reconfiguration methodologies and deployment strategies in practical scenarios have not been well-studied so far. Among these challenges, the physical characteristics remain urgent to be modeled and clarified, which are the basis of other effective extensions.

In the early literature, RIS is usually described as an anomalous mirror that reflects impinging plane waves as outgoing plane waves with an unnatural angle (which is different from the specular angle predicted by Snell’s Law). Recently, it has been clarified by [3] that neither the plane wave nor infinite surface area will typically appear in practice, thus they are regarded as theoretical idealizations for RIS. And the authors illustrated by simulations that an RIS of finite size can generally not be interpreted as a mirror when impinged by plane waves.

J. Hu, H. Yin, L. Tan, L. Cao and X. Pei are with Huazhong University of Science and Technology, 430074 Wuhan, China. (e-mail: {jiangfenghu, yin, ltan, caolin, pei}@hust.edu.cn. The corresponding author is Li Tan.

This work was supported in part by the National Key Research and Development Program of China under Grant 2020YFB1806904, in part by the National Natural Science Foundation of China under Grants 62071191, 62071192, and 1214110.

It is interesting to think, what will actually happen if a spherical wave (or even a beam) is impinging on a finite-sized RIS? The authors of [4] validated by experimental measurements that an RIS configured to uniform state with high scattering efficiency has similar characteristics as a metal plate with the same shape and size. However, the transceivers in [4] are placed in the far-field of the RIS operating in millimeter-wave bands, and there is lack of the comparisons between the well-rotated metal plate and a smartly-configured RIS, which is a relatively more general application scenario for RIS [2]. In fact, some researchers suggest we may carefully employ “fully-passive RIS” (e.g., the metal plate) in some specific scenarios where the EM environment is quasi-static to further reduce the hardware and energy overhead. The paper [5] indicated that a well-rotated metal plate is as efficient as RIS under the far-field assumption. What if the array grows large enough relative to the communication distance thus we are in the near-field of RIS array? To the best of our knowledge, there is still a lack of experimental validations in the literature whether or to what extent a well-configured RIS can be replaced with a well-rotated “fully-passive RIS” of the same shape and size, especially when impinged by spherical waves. In view of the conditions above, the main contributions of this paper are:

- Based on the wave optics theory, we establish explicit scattering efficiency models for both the RIS and the metal plate, which are represented by the concept of radar cross section (RCS), and extend the standard bistatic RCS [6] of a rectangle plate to more general cases.
- We verify the the proposed models by simulation and field measurements. The measurement results are in good agreement with the simulation results predicted by the proposed models.
- We validate by both simulation and measurement results that a well-configured RIS can outperform a well-rotated metal plate of the same size in most practical cases, which indicates the power-focusing superiority of RIS.

Notations: We use uppercase and lowercase bold-face variables to denote matrices and vectors, respectively. $\mathbf{r} = x\hat{\mathbf{x}} + y\hat{\mathbf{y}} + z\hat{\mathbf{z}}$ is a vector with Cartesian coordinates (x, y, z) , and $\hat{\mathbf{r}} = \text{uni}(\mathbf{r})$, which is the unitization form of \mathbf{r} representing its direction. $\|\mathbf{r}\|$ and \mathbf{r}^* denote the Frobenius norm and the conjugate transpose of \mathbf{r} , respectively. ∇ is the nabla operator, and $\nabla_{\mathbf{r}}$ denotes the gradient evaluated at the \mathbf{r} vector. \cdot and \times denote the scalar and vector products between vectors, respectively, and \mathbf{I} is the identity matrix.

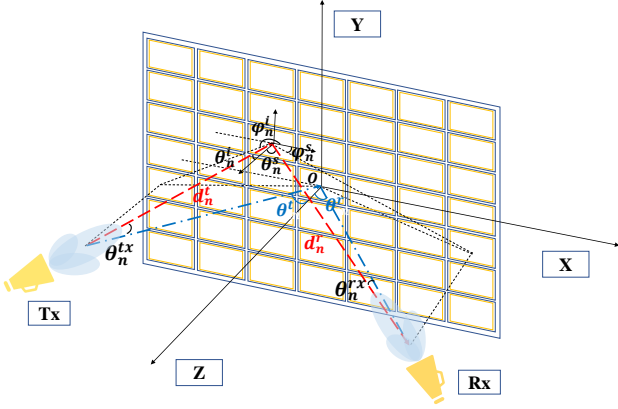


Fig. 1: The geometric illustration of an RIS-aided communication system.

II. SYSTEM MODEL

We consider an RIS-aided communication system in three-dimensional (3D) space. For ease of exposition and experiments, the transmitter (Tx) and the receiver (Rx) are both equipped with a single antenna. The generalization of the proposed model to multiple antenna settings is straightforward. The above settings are consistent in both simulation and field measurement experiments. The Tx, Rx and RIS are placed in a Cartesian coordinate system, as shown in Fig. (1), whose locations Tx and Rx are denoted as \mathbf{p}_t , \mathbf{p}_r and \mathbf{p}_r , respectively.

Without loss of generality, we place the RIS of a rectangle shape with $N_v \times N_h$ elements on the xOy -plane, with its geometric center aligned with the origin, where N_v and N_h denote the number of columns and rows of RIS elements. The two sides of the RIS are placed in parallel to the x -axis and y -axis. The element cells are designed to be edge-to-edge thus the vertical (horizontal) distance between their geometric centers (i.e., the spatial period) is exactly the width (length) of a single RIS element cell, denoted by d_v and d_h , respectively. For more design details, we refer the interested readers to our previous work [7]. We denote the n -th RIS element located at \mathbf{p}_n by C_n , $n = 1, \dots, N_v N_h$.

We assume the Tx and Rx are always in the element far-field, instead of the array far-field [8]. This usually makes sense at a normal communication distance, which is long enough relative to the sub-half-wavelength element size. For simplicity, the mutual coupling effect is not considered. Therefore, the impinging EM waves can be regarded (approximately) as plane waves for a particular RIS element and we can exploit the signals scattered by each independent element to calculate the signal at the receiver side. For a single RIS element C_n , we model its scattering factor S_n as the combination of an inherent part and a reconfigurable part as:

$$S_n(\hat{\mathbf{r}}_n^i, \hat{\mathbf{r}}_n^s, u_n) = f_n(\hat{\mathbf{r}}_n^i, \hat{\mathbf{r}}_n^s) R_n(u_n), \quad (1)$$

where $f(\hat{\mathbf{r}}_n^i, \hat{\mathbf{r}}_n^s)$ is the inherent part (i.e., the original element scattering characteristics) formulated by a bidirectional scattering distribution (BSD) function which will be derived and discussed in details later. $\hat{\mathbf{r}}_n^i = \text{uni}(\mathbf{p}_n - \mathbf{p}_t)$, $\hat{\mathbf{r}}_n^s = \text{uni}(\mathbf{p}_r - \mathbf{p}_n)$ denote the direction of the incident wave, the direction of the

scattered wave, respectively. The reconfigurable part

$$R_n(u_n) = \alpha_n(u_n) e^{-j\phi_n(u_n)} \quad (2)$$

is determined by the on-board control signal u_n (e.g., a biasing voltage that can be properly selected), where α_n and ϕ_n represent the amplitude and phase response, respectively. Therefore, if we denote the transmit signal by x , the received signal reflected by a single RIS element C_n can be formulated as $y_n = g_n S_n h_n x$, where h_n and g_n denote the channel coefficient between the Tx and C_n , the channel coefficient between C_n and the Rx, respectively. Take h_n for example, the channel coefficient can be formulated by $h_n = \beta_n e^{-j2\pi \frac{d_n^{tx}}{\lambda}}$, where λ is the wave length and d_n^{tx} is the distance between the Tx and the RIS element C_n . And $\beta_n = \sqrt{\beta_0 \cos \theta_n^{tx} / 4\pi (d_n^{tx})^\gamma}$ represents the path-loss factor, where β_0 and γ are constant depending on the communication environment, θ_n^{tx} is the angle between Tx-O and Tx- C_n to account for the effect of antenna directivity [9], as shown in Fig. 1. The channel coefficient g_n can be formulated similarly.

III. MODELING OF THE RECEIVED SIGNAL

In this section, we model and analyze the received signal that is reflected by either a metal plate or an RIS. In the following context, we adopt the term *diffraction* to emphasize the scattering at the edges of an element cell. And these edges usually occur when material discontinuity exists, which may lead to the spatial distribution discontinuities of permittivity and permeability.

As analyzed in [10], for a perfectly conducting rectangular plate, the radar cross section is an appropriate parameter to depict its scattering efficiency in the given directions. RCS is originally defined as the ratio of the incident and scattered electric field power (or equivalently the magnetic field power) and can be formulated as: $\sigma = \lim_{R \rightarrow \infty} \left(4\pi R^2 |\mathbf{E}^s|^2 / |\mathbf{E}^i|^2 \right)$, where \mathbf{E}^i and \mathbf{E}^s denote the incident and scattering electric field, respectively, and R is the distance between the source and the geometric center of the plate.

The formula above inherits the far-field assumption. Nevertheless, one of the main advantages of RIS is the nearly-passive characteristic, which enables it to have a larger array size than the massive MIMO setups to interact with more EM waves propagating in wireless environment [11]. Therefore, sometimes the transceivers will inevitably be in the near field of the whole RIS array, and a direct application of the definition above may not be always appropriate in our experiments. Fortunately, though we may not always in the far field of the whole surface, we will be in the far field of the element in most cases. For fair comparison, we discretize the metal plate in the same way as our designed RIS prototype (i.e., same number of cell, equal cell size) and calculate the RCS on each element cell separately before summing them up. Note that it is a common operation in the literature of RCS, where a continuous surface is divided into a collection of small discrete patches [12]. Under these assumptions, first we have the following theorem for the metal cell:

Theorem 1: *Within the element far-field regions, the RCS of a single metal cell M_n under the given incident angle and*

observation angle is formulated as:

$$\sigma_n^M(\hat{\mathbf{r}}_n^i, \hat{\mathbf{r}}_n^s) = 4\pi (d_v d_h / \lambda)^2 \cos^2 \theta_n^i \cdot (\cos^2 \theta_n^s \cos^2 \varphi_n^s + \sin^2 \varphi_n^s) (\sin(X)/X)^2 (\sin(Y)/Y)^2. \quad (3)$$

where θ_n^i (φ_n^i), θ_n^s (φ_n^s) denote the elevation (azimuth) angle of the incident wave, the elevation (azimuth) angle of the scattered wave relative to the element C_n , respectively. X and Y are defined in (17) and (18), respectively.

Proof: The derivations are given in Appendix A. \square

It can be inferred from the result above that the RCS of a metal cell is related to the wave propagation direction, the observation direction, and the metal cell inherent properties like its aspect ratio and the size relative to the wavelength. In addition, once the direction of observation is determined, the scattered power is relatively larger near the specular direction (i.e., $\theta_n^i = \theta_n^s$, $\varphi_n^i = \varphi_n^s + \pi$) and the scattering efficiency will increase when the direction is closer to the boresight of the plate. Thus the received power will be maximized when these two directions are matched, i.e., the waves are transmitted and received along the boresight of the plate.

Since RCS is a parameter originally describing the attenuation ratio between the incident and scattered power, its effect on the transmitting signal can be derived as $f_n^M(\hat{\mathbf{r}}_n^i, \hat{\mathbf{r}}_n^s) = \sqrt{\sigma_n^M(\hat{\mathbf{r}}_n^i, \hat{\mathbf{r}}_n^s)}$, which is the BSD function we mentioned in the previous section. Thus, the receive signal scattered by the whole metal plate can be formulated as

$$y^M = \sum_{n=1}^{N_v N_h} h_n f_n^M(\hat{\mathbf{r}}_n^i, \hat{\mathbf{r}}_n^s) g_n x. \quad (4)$$

When it comes to the case of RIS, the element structure is relatively more complicated than that of a metal cell, which leads to a more complex formulation representing its scattering characteristics. Specifically, on the surface of an RIS with practically discretized configurations, there are inevitably material discontinuities between copper coats and substrates within elements [7], which will cause spatial distribution discontinuities of the permittivity and permeability [13], resulting in the edge diffraction of the incident waves. What is more, the control signal (e.g., external bias voltage for varactor diode based-RIS) applied on each RIS element will bring an extra impedance change. Thus, compared with a metal cell, additional phase and amplitude responses will appear on the RIS element. However, according to our design experience, the RIS element structure is usually designed flexibly to adapt to the working frequency bands and application requirements. In Corollary 1, we provide an adjusted RCS for RIS element in order to establish a simple yet general scattering model:

Corollary 1: *Within the element far-field regions, the RCS of a single RIS element C_n under the given incident angle and observation angle can be formulated as:*

$$\sigma_n^R(\mathbf{r}_n^i, \mathbf{r}_n^s) = 4\pi (d_v d_h / \lambda)^2 (\sin(X)/X)^2 (\sin(Y)/Y)^2 \cdot (\cos^2 \theta_n^i) (\cos^2 \theta_n^s \cos^2 \varphi_n^s + \sin^2 \varphi_n^s) \mathcal{D}_n(\mathbf{r}_n^i, \mathbf{r}_n^s) \quad (5)$$

where

$$\mathcal{D}_n(\mathbf{r}_n^i, \mathbf{r}_n^s) = 1 - \mu \sin((\theta_n^i + \theta_n^s)/2) \cos(kd_v((\sin \theta_n^i + \sin \theta_n^s)/2)). \quad (6)$$



Fig. 2: The testing and measurement scenarios.

k is the wavenumber, μ is the diffraction loss factor describing energy loss ratio due to diffraction (depending on the medium types at the edges), and the meanings of other parameters are aligned with Theorem 1.

Proof: Based on eq. (3), it is proposed with an additional diffraction component to depict the edge diffraction effects of the RIS element, which is inspired from the first principle in [14]: the diffraction effects mainly depend on the elevation angles, which are more evident when approaching grazing direction (i.e., $\theta_n^i = \pi/2$ and $\theta_n^s = \pi/2$). \square

Accordingly, the BSD of the RIS element C_n is derived as $f_n^R(\mathbf{r}_n^i, \mathbf{r}_n^s) = \sqrt{\sigma_n^R(\mathbf{r}_n^i, \mathbf{r}_n^s)}$. Finally, the received signal scattered by the whole RIS plane is:

$$y^R = \sum_{n=1}^{N_v N_h} h_n R_n(u_n) f_n^R(\mathbf{r}_n^i, \mathbf{r}_n^s) g_n x. \quad (7)$$

IV. EXPERIMENTAL RESULTS AND ANALYSIS

In this section, we start by briefly introducing our experimental configuration and then validate the power focusing capability of RIS, as well as our proposed models of the received signal. Fig. 2 illustrates the measurement environments. The basic parameters of our field measurements and details of the RIS platform can be found in our previous work [7]. Before the experiments, we have calibrated the system by aligning the transmit and receive antenna under a line-of-sight setting.

Since the configuration goal is to focus signals at the receiver side, here we iterate the algorithm introduced in [7] for several times to approach the optimal configuration. To prove experimentally the power focusing superiority of RIS, we compare the received power with the assistance of RIS and that of a same-sized well-rotated metal plate under several different scenarios. As depicted in Fig. 1, θ^t and θ^r denotes the zenith angle from the origin to the Tx, the zenith angle from the origin to the Rx, respectively. Since we are interested in the comparisons that are most effective for the metal plate to enhance the receiving signals, we always set the two angles to be identical in the subsequent content, as shown in Fig. 2.

The model proposed in [4] considered several factors that impact the received power in RIS-assisted system, which is

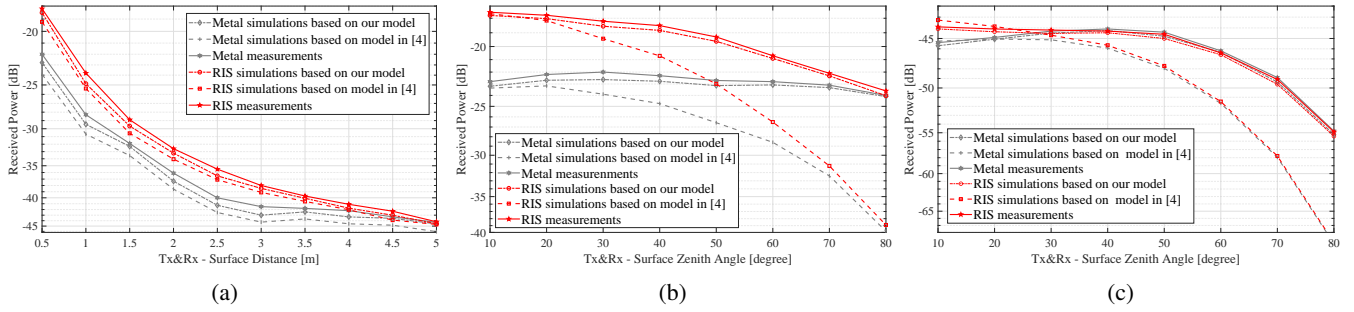


Fig. 3: (a) Received power versus the Tx&Rx - Surface distances at 30 degree zenith angle. (b) Received power versus the zenith angles, the Tx&Rx - surface distances are 50 cm. (c) Received power versus the zenith angles, the Tx&Rx-surface distances is 5 m.

suitable to be adopted here for comparisons. Their normalized power radiation pattern for each unit can be equivalently rewritten in the form of RCS as [4] (notations have been modified to be consistent with our paper): $\sigma_n^C(\hat{\mathbf{r}}_n^i, \hat{\mathbf{r}}_n^s) = \cos^2\theta_n^i \cos^2\theta_n^s$. Thus, by squaring the received signal and adding the normalization factor, the total received power can be formulated as in [15]:

$$P_r = \frac{P_t \lambda^2}{4\pi} \left| \sum_{n=1}^{N_v N_h} h_n R_n \sqrt{\sigma_n} g_n \right|^2 \quad (8)$$

For fair comparison, other factors except for the RCS item are set to be the same for different models in [4] and ours. And for the metal plate, the coefficient R_n is set to 1.

Fig. 3(a) shows the measurement results and the simulation results based on the proposed models at the specular zenith angle of 30 degree (i.e., $\theta^t = \theta^r = 30^\circ$) and the same Tx&Rx-surface distances. It mainly illustrates the relationship between the received power and the communication distances. We can observe that within the border between near field and far field of RIS ($\frac{2N_v N_h d_v d_h}{\lambda} \simeq 6$ m) [9], as the Tx-surface and Rx-surface distances increase simultaneously, the received power of the RIS-aided system is always higher due to the focalization of RIS, yet decreases faster than the metal-aided one. The focusing superiority of RIS gradually disappears as the distances approach 5 m, which makes sense since the phase shifts (seen from both the Tx and the Rx) between the surface center and edges will decrease rapidly as the distances increase. Moreover, the relative side lobe level (RSL) of a well-configured RIS will decrease with distance, which also impacts the focusing ability of it. The measurement results have similar trend with simulation results based on our model, however with a slight increase which might result from the multi-path effect caused by scatterers in the environment.

Fig. 3(b) shows the measurement results and the simulation results based on the proposed models at Tx&Rx - surface distances of 50 cm. It mainly illustrates the relationship between the zenith angles and the received power. We can observe that the received power of both RIS and metal plate assisted system decrease as the zenith angles deviated from the boresight and the former decreases faster. It is in line with our expectation since their scattering efficiency (represented by the RCS) will decrease in a similar manner. Within such a short distance, the focusing ability of RIS is obvious for most angles. This

is because the phase differences over the scattering surface are relatively large, and most of the transmitting power can be utilized here, thus the reconfigurable phase shifts (which determine the actual scattering direction) of RIS is more important than a little higher RCS of the metal plate.

When we increase the Tx-surface and RX-surface distances to 5 m, as shown in Fig. 3(c), it is interesting that the focusing ability of RIS still exists at small zenith angles. And the received power curves of the RIS and the metal plate aided systems begin to cross as the angle increases. Several causes may lead to this result. First, the maximum scattering efficiency (usually occurs in a small zenith angle) of RIS and the metal plate is different. Second, as mentioned above, the scattering efficiency of RIS will decrease faster as the zenith angles increase due to its edge diffraction phenomenon. Furthermore, at the relatively longer distances, the phase differences are more difficult to distinguish, which is not beneficial for RIS to focus signals.

V. CONCLUSION

In this paper, novel scattering models based on wave optics theory have been derived and explicitly formulated for both the metal plate and the RIS. The simulation results from these models showed good agreements with the field measurement results, which indicated the effectiveness of the proposed models. And we validated the power focusing superiority of a well-configured RIS by both simulation and measurement results, proved that it outperforms a well-rotated metal plate with the same shape and size in most cases, especially at relatively close distance and small zenith angle from the transceivers.

APPENDIX A PROOF OF THEOREM 1

Proof: In the following, footmarks indicating specific units are temporarily dropped to make the text more concise. Consider a point source located at $\mathbf{p}_t = x_t \hat{\mathbf{x}} + y_t \hat{\mathbf{y}} + z_t \hat{\mathbf{z}}$ generates an incident electric field $\mathbf{E}^{in}(\mathbf{p}_t, \mathbf{r})$ at the n -th element cell located at $\mathbf{r} = x \hat{\mathbf{x}} + y \hat{\mathbf{y}} + z \hat{\mathbf{z}}$. The incident wave can be given by the tensor Green's function $\mathbf{G}(\mathbf{r})$, the resulting wave at \mathbf{r} is

$$\mathbf{E}^{in}(\mathbf{p}_t, \mathbf{r}) = \mathbf{G}(\mathbf{r} - \mathbf{p}_t) \mathbf{J}^t(\mathbf{p}_t), \quad (9)$$

where $\mathbf{J}^t(\mathbf{p}_t)$ is the monochromatic source current. And since the EM waves our practical system adopt is linearly polarized wave, we accordingly assume here only the x direction of the current is excited at the source. Due to the fact that we may always in the far field of a sub-wavelength element cell, the wave arrives at the element is approximately a plane wave, thus we mainly focus on its phase shift over the element and assume a uniform amplitude E_0^{in} . Let $\mathbf{k}(\mathbf{p}_t, \mathbf{r})$ denote the wavevector of the incident wave:

$$\mathbf{k}(\mathbf{p}_t, \mathbf{r}) = k(\sin\theta_i \cos\varphi_i \hat{\mathbf{x}} + \sin\theta_i \sin\varphi_i \hat{\mathbf{y}} - \cos\theta_i \hat{\mathbf{z}}), \quad (10)$$

which identifies the direction of the incident wave and θ_i (φ_i) denote the elevation (azimuth) angle of it. Therefore, the incident electric field can be formulated as

$$\mathbf{E}^{in}(\mathbf{p}_t, \mathbf{r}) = E_0^{in} e^{-jk(\sin\theta_i \cos\varphi_i x + \sin\theta_i \sin\varphi_i y - \cos\theta_i z)} \hat{\mathbf{x}}. \quad (11)$$

Then, by applying Maxwell's equations, the incident magnetic field can be obtained as

$$\begin{aligned} \mathbf{H}^{in}(\mathbf{p}_t, \mathbf{r}) &= -\frac{1}{j\omega\mu_0} \nabla_{\mathbf{r}} \times \mathbf{E}^{in}(\mathbf{p}_t, \mathbf{r}) \\ &= -\frac{E_0^{in}}{\eta_0} (\cos\theta_i \hat{\mathbf{y}} + \sin\theta_i \sin\varphi_i \hat{\mathbf{z}}) \\ &\quad \cdot e^{-jk(\sin\theta_i \cos\varphi_i x + \sin\theta_i \sin\varphi_i y - \cos\theta_i z)}, \end{aligned} \quad (12)$$

where ω is the angular frequency of the wave, μ_0 and η_0 denote the permittivity and impedance of free-space, respectively. Note that the element cells are all located on the xOy plane (i.e., $z = 0$), and we temporarily drop the arguments in $\mathbf{H}^{in}(\mathbf{p}_t, \mathbf{r})$ to lighten the notations:

$$\begin{aligned} \mathbf{H}^{in} &= \mathbf{H}^{in}(\mathbf{p}_t, \mathbf{r}) \Big|_{z=0} \\ &= -\frac{E_0^{in}}{\eta_0} (\cos\theta_i \hat{\mathbf{y}} + \sin\theta_i \sin\varphi_i \hat{\mathbf{z}}) e^{-jk(\sin\theta_i \cos\varphi_i x + \sin\theta_i \sin\varphi_i y)}. \end{aligned} \quad (13)$$

Since the metal plate is a kind of good conductor whose thickness is negligible here, the equivalent current density at the incident point can be approximated as twice the amplitude of the incident tangential magnetic field components [12]:

$$\begin{aligned} \mathbf{J}^s &\simeq 2\hat{\mathbf{n}} \times \mathbf{H}^{in} \Big|_{\substack{x=x' \\ y=y'}} \\ &= 2\frac{E_0^{in}}{\eta_0} \cos\theta_i e^{-jk(\sin\theta_i \cos\varphi_i x' + \sin\theta_i \sin\varphi_i y')} \hat{\mathbf{x}}, \end{aligned} \quad (14)$$

where $\hat{\mathbf{n}}$ is the the unit surface normal. Therefore, by applying the above equation and adopting the auxiliary variables of vector potential defined in [6], we can obtain that

$$\begin{aligned} N_\theta &= \int \int_S \left(J_x^s \cos\theta_s \cos\varphi_s + J_y^s \cos\theta_s \sin\varphi_s - J_z^s \sin\theta_s \right) \Big|_{\substack{J_y^s=0 \\ J_z^s=0}} \\ &\quad \cdot e^{-jk(\sin\theta_i \cos\varphi_i x' + \sin\theta_i \sin\varphi_i y')} dx' dy' \\ &= 2d_v d_h \frac{E_0^{in}}{\eta_0} [\cos\theta_i \cos\theta_s \cos\varphi_s (\sin(X)/X) (\sin(Y)/Y)], \end{aligned} \quad (15)$$

$$\begin{aligned} N_\varphi &= \int \int_S \left(-J_x^s \sin\varphi_s + J_y^s \cos\varphi_s \right) \Big|_{J_y^s=0} \\ &\quad \cdot e^{-jk(\sin\theta_i \cos\varphi_i x' + \sin\theta_i \sin\varphi_i y')} dx' dy' \\ &= 2d_v d_h \frac{E_0^{in}}{\eta_0} [\cos\theta_i \sin\varphi_s (\sin(X)/X) (\sin(Y)/Y)], \end{aligned} \quad (16)$$

where θ_s (φ_s) denote the elevation (azimuth) angle of the scattered wave, and

$$X = \frac{\pi d_v}{\lambda} (\sin\theta_s \cos\varphi_s + \sin\theta_i \cos\varphi_i), \quad (17)$$

$$Y = \frac{\pi d_h}{\lambda} (\sin\theta_s \sin\varphi_s + \sin\theta_i \sin\varphi_i). \quad (18)$$

Therefore, we can obtain the amplitude components of the scattered electric field as:

$$|E_\theta^s| = \frac{k d_v d_h E_0^{in}}{2\pi r} [\cos\theta_i \cos\theta_s \cos\varphi_s (\sin(X)/X) (\sin(Y)/Y)], \quad (19)$$

$$|E_\varphi^s| = \frac{k d_v d_h E_0^{in}}{2\pi r} [\cos\theta_i \sin\varphi_s (\sin(X)/X) (\sin(Y)/Y)]. \quad (20)$$

Finally, by adopting (11) and the original RCS definition, as well as $|E^s| = \sqrt{|E_\theta^s|^2 + |E_\varphi^s|^2}$, we can obtain the RCS of a metal plate of size $d_v \times d_h$ as:

$$\begin{aligned} \sigma^M &= 4\pi \left(\frac{d_v d_h}{\lambda} \right)^2 \cos^2\theta_i (\cos^2\theta_s \cos^2\varphi_s + \sin^2\varphi_s) \cdot \\ &\quad (\sin(X)/X)^2 (\sin(Y)/Y)^2. \end{aligned} \quad (21)$$

Thus Theorem 1 is proved. \square

REFERENCES

- [1] C. Huang, A. Zappone, G. C. Alexandropoulos, M. Debbah, and C. Yuen, "Reconfigurable intelligent surfaces for energy efficiency in wireless communication," *IEEE Trans. Wireless Commun.*, vol. 18, no. 8, pp. 4157–4170, 2019.
- [2] Y. Liu, X. Liu, X. Mu, T. Hou, J. Xu, M. Di Renzo, and N. Al-Dahir, "Reconfigurable intelligent surfaces: Principles and opportunities," *IEEE Commun. Surveys Tuts.*, 2021.
- [3] E. Björnson, Ö. Özdogan, and E. G. Larsson, "Reconfigurable intelligent surfaces: Three myths and two critical questions," *IEEE Commun. Mag.*, vol. 58, no. 12, pp. 90–96, 2020.
- [4] W. Tang, X. Chen, M. Z. Chen, J. Y. Dai, Y. Han, M. D. Renzo, S. Jin, Q. Cheng, and T. J. Cui, "Path loss modeling and measurements for reconfigurable intelligent surfaces in the millimeter-wave frequency band," *IEEE Trans. Commun.*, vol. 70, no. 9, pp. 6259–6276, 2022.
- [5] Ö. Özdogan, E. Björnson, and E. G. Larsson, "Intelligent reflecting surfaces physics, propagation, and pathloss modeling," *IEEE Wireless Commun. Lett.*, vol. 9, no. 5, pp. 581–585, 2019.
- [6] C. A. Balanis, *Advanced engineering electromagnetics*. John Wiley & Sons, 2012.
- [7] X. Pei, H. Yin, L. Tan, L. Cao, Z. Li, K. Wang, K. Zhang, and E. Björnson, "RIS-aided wireless communications: Prototyping, adaptive beamforming, and indoor/outdoor field trials," *IEEE Trans. Commun.*, vol. 69, no. 12, pp. 8627–8640, 2021.
- [8] J. C. B. Garcia, A. Sibille, and M. Kamoun, "Reconfigurable intelligent surfaces: Bridging the gap between scattering and reflection," *IEEE J. Sel. Areas Commun.*, vol. 38, no. 11, pp. 2538–2547, 2020.
- [9] W. Tang, M. Z. Chen, X. Chen, J. Y. Dai, Y. Han, M. Di Renzo, Y. Zeng, S. Jin, Q. Cheng, and T. J. Cui, "Wireless communications with reconfigurable intelligent surface: Path loss modeling and experimental measurement," *IEEE Trans. Wireless Commun.*, vol. 20, no. 1, pp. 421–439, 2021.
- [10] E. F. Knott, J. F. Schaeffer, and M. T. Tuley, *Radar cross section*. SciTech Publishing, 2004.
- [11] E. Björnson and L. Sanguinetti, "Power scaling laws and near-field behaviors of massive MIMO and intelligent reflecting surfaces," *IEEE IEEE Open J. Commun. Soc.*, vol. 1, pp. 1306–1324, 2020.
- [12] M. I. Skolnik, *Radar handbook*. McGraw-Hill, 1970.
- [13] P. Ufimtsev, "Comments on diffraction principles and limitations of RCS reduction techniques," *Proc. IEEE*, vol. 84, no. 12, pp. 1830–1851, 1996.
- [14] R. Ross, "Radar cross section of rectangular flat plates as a function of aspect angle," *IEEE Trans. Antennas Propag.*, vol. 14, no. 3, pp. 329–335, 1966.
- [15] M. Di Renzo, A. Ahmed, A. Zappone, V. Galdi, G. Gradoni, M. Moccia, and G. Castaldi, "Digital reconfigurable intelligent surfaces: On the impact of realistic reradiation models," 2022. [Online]. Available: <https://arxiv.org/abs/2205.09799>